Analysis of Broadband Solar Radiation and Albedo over the Ocean Surface at COVE

ZHONGHAI JIN

Analytical Services & Materials, Inc., Hampton, Virginia

THOMAS P. CHARLOCK

Atmospheric Sciences Division, NASA Langley Research Center, Hampton, Virginia

KEN RUTLEDGE

Analytical Services & Materials, Inc., Hampton, Virginia

(Manuscript received 9 October 2001, in final form 29 March 2002)

ABSTRACT

A coupled atmosphere–ocean radiative transfer model has been applied to analyze a full year of broadband solar irradiances (up and down) measured over an ocean site 25 km east of the coast of Virginia in the Atlantic. The coupled model treats absorption and scattering by layers for both the atmosphere and the ocean explicitly and consistently. Key input parameters for the model (aerosol optical depth, wind speed, and total precipitable water) are also from in situ measurements. Having more observations to specify properties of the atmosphere than of the ocean, better model–observation agreement is obtained for the downwelling irradiance, which depends primarily on the atmospheric optical properties, than for the upwelling irradiance, which depends heavily on the ocean optical properties. The mean model–observation differences for the ocean surface albedo are generally less than 0.01. However, the modeled upwelling irradiances and albedo over the ocean surface are mostly less than the observations for all seasons, implying that more scattering in the ocean needs to be included in the model calculations. Sensitivity tests indicate that the uncertainties in aerosol optical properties, chlorophyll concentration, wind speed, or foams are not the primary factors for the model–observation differences in the ocean surface albedo, whereas the scattering by air bubbles and/or by suspended materials have the potential to significantly reduce or eliminate the model–observation differences in the ocean surface reflection.

1. Introduction

Radiation and its spatial and temporal variations drive the general circulation and the hydrological cycle. One of the major sources of uncertainty in climate prediction lies in the radiative energy flow through the earth–atmosphere system and the radiative interactions between the atmosphere and the hydrosphere. The radiative energy budget is the most important component of the air–sea energy flux. In particular, the shortwave solar energy accounts for most of the heat flux transferred into the ocean. The absorption of solar radiation by the upper layers affects the stratification and stability of the ocean mixed layer, the sea surface temperature, and the general circulation of the ocean. Because solar radiation is the energy source for photosynthesis, it influences marine primary productivity directly, and impacts cascade throughout ocean ecosystems.

The surface radiation budget has long been recognized as fundamental to our understanding of the climate system (Houghton et al. 1996). Surface radiation measurements are essential for the validation of both radiative transfer models and flux retrieval algorithms using satellite data. Hence ground stations have been established to monitor the radiative budget. This has led to a series of comparisons between models and measurements (e.g., Kinne et al. 1998; Conant et al. 1997; Chou and Zhao 1997; Charlock and Alberta 1996; Kato et al. 1997). However, most measurements are over inhabited areas, and routine observations over the ocean are extremely limited. It is difficult to make accurate surface radiation measurements from a moving platform such as a ship or buoy. A team led by one of us (K.R.) recently installed a set of instruments on a rigid platform over the ocean to measure radiation and the air and sea states. To analyze the measurements, we applied a coupled atmosphere–ocean radiative transfer model. Unlike typical models that treat radiative transfer in the atmosphere and ocean separately (often by regarding one medium simply as a boundary condition for the other), the coupled model considers the absorption and scattering in the atmosphere and in the ocean explicitly and consistently. Such a model is capable of more accurately calculating the upwelling flux and albedo over the ocean surface based on the optical properties in the atmosphere and ocean.

Corresponding author address: Dr. Zhonghai Jin, Analytical Services and Materials, Inc., 1 Enterprise Parkway, Suite 300, Hampton, VA 23666.
E-mail: z.jin@larc.nasa.gov

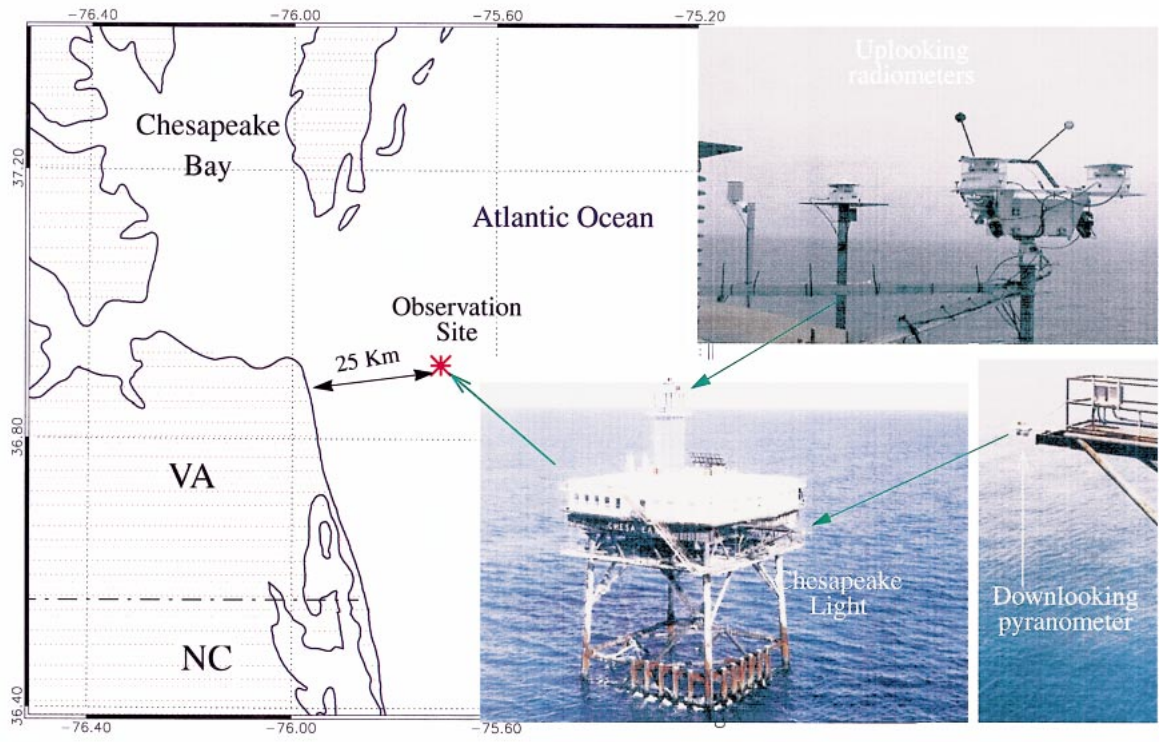

FIG. 1. Illustration of the radiation measurement platform and location.

The surface of the ocean is the most ubiquitous boundary condition for solar radiation that enters the earth atmosphere system. How realistically does present theory ''close'' that boundary condition? The application of satellite observations of broadband top of the atmosphere (TOA) albedo for aerosol forcing (and for parsing absorption by the surface vs the atmosphere) is contingent upon the answer. Our main goal here is a comparison of the broadband albedo observed at the ocean surface with theory. In this paper, we will apply the coupled atmosphere–ocean radiative transfer model to analyze a full year of broadband downwelling and upwelling irradiances at the CERES Ocean Validation Experiment (COVE) site. In the next sections, we will briefly introduce the observation data and the model. Then the data will be analyzed and compared to the model. Finally, the results will be discussed.

2. Measurement and data

The investigation of Clouds and the Earth's Radiant Energy System (CERES), which is a key part of the National Aeronautics and Space Administration (NASA) Earth Observing System, is intended to substantially improve our understanding of energetically significant radiation, clouds, and the interaction between the two. CERES continues the Earth Radiation Budget Experiment record of radiative fluxes at the TOA, and aims to improve our knowledge of the earth's surface radiation budget by providing a long-term climatology of surface radiation fluxes based on well-calibrated satellite observations and a comprehensive retrieval algorithm. To develop and validate the retrieval algorithms for surface fluxes, and tighten closure on atmospheric fluxes and related forcings with TOA CERES observations, a measurement site, COVE, was established close to the mouth of Chesapeake Bay off the coast of Virginia (Fig. 1).

The instruments and their measured or derived properties at COVE are listed in Table 1. Routine radiation measurements at the COVE site include broadband shortwave and longwave, downwelling, and upwelling irradiances. The downwelling broadband shortwave radiation measurements include the direct and diffuse components and their global composite (using a pyrheliometer, and shaded and unshaded pyranometers, respectively). Narrowband global and diffuse measurements are made using a multifilter rotating shadowband radiometer (MFRSR); direct spectral components are then inferred to determine wavelength specific extinction and aerosol optical thickness within the atmosphere. Spectral extinction is also directly measured using a classical sun photometer (NASA's AERONET Cimel instrument) (Holben et al. 1998). The Cimel sun photometer also makes periodic almacantur and solar principal plane atmospheric radiance scan measurements for aerosol phase function and particle size determinations. Upwelling spectral ocean surface radiance field measure-

TABLE 1. Instruments and measurements at COVE.

Instrument	Parameters measured/derived	Spectral characteristics
Kipp & Zonen CH1 pyranometer	Direct solar irradiance*	Broadband (0.2–4.0 μm)
Shaded Kipp & Zonen CH31 pyranometer	Downwelling diffuse shortwave irradiance*	Broadband (0.2–4.0 μm)
Epply PSP pyranometer	Upwelling shortwave irradiance*	Broadband (0.28–4.0 μm)
Yankee Environmental Systems MFRSR	Narrowband direct, diffuse, global shortwave irradiances	Center wavelengths at 415, 500, 615, 670, 870, 936 nm
Schulz SP1A spectroradiometer	Narrowband radiance	Narrowband
NOAA GPS network	Precipitable water*	
NOAA meteorology station at COVE	Wind speed/direction,* temperature, pressure, humidity	
NASA AERONET (Cimel) sun photometer	Aerosol optical properties,* size distribution, refractive indice	Center at 340,380, 440, 500, 670, 870, 1020 nm
Eppley PIR pyrgeometer	Infrared irradiances	Broadband (3.5–50.0 μm)

* Parameters used in the study.

ments are made using a scanning, high dynamic range sun photometer (Schulz and Partners, GmBH, model SP1A). The SP1A photometer has been calibrated using the 6-ft-diameter radiance calibration integrating sphere at NASA's Goddard Space Flight Center. Integrated precipitable water (PW) is measured using a dual-frequency global positioning system instrument by the National Oceanic and Atmospheric Administration (NOAA) GPS Demonstration network. Standard meterological parameters (wind speed/direction, temperature, pressure, humidity) are measured at several heights above the water level. Ocean surface wave energy spectra are derived from a high-frequency wave height sensor developed by NOAA's National Data Buoy System, which also measures meteorological parameters.

In this paper, an entire year (1 March 2000–1 March 2001) of data for the broadband solar radiation was analyzed. During this period, the broadband direct beam was measured by a Kipp and Zonen (KZ) model CH1 pyrheliometer; the shaded pyranometer measuring downwelling diffuse radiation was a KZ model CM31; the unshaded pyranometer measuring global downwelling was also a KZ model CM31; the pyranometer measuring upwelling was an Eppley model Precision Spectral Pyranometer, fitted with a yellow shield that obscured 5° from the horizon. Instruments for measuring broadband downwelling were mounted at the highest level (37 m ASL) on the tower of COVE (Fig. 1). The pyranometer measuring upwelling flux was fitted to a boom (displaced horizontally 6.7 m from the main platform and 21.3 m above the sea surface), which projected toward 245°N. The platform fixture (a steel leg) closest to the point on the sea directly beneath the boom pyranometer made an angle of 26° from the horizontal (for perspective, said point on the sea made an angle of 90° with the horizontal). An automatic washing device cleaned the pyrheliometer window each day. Our experience indicated that the pyrheliometer (which takes a collimated measurement) was more susceptible to corruption by dust, etc., than the other broadband instruments (which each measure over an entire hemisphere). Window and dome obscuration by sea spray at COVE are much less than at a coastal beach. The nearest beach and its breaking surf are 25 km to the west of COVE. Larger sea spray particles apparently do not reach the level of our lowest instruments (~20 m) frequently.

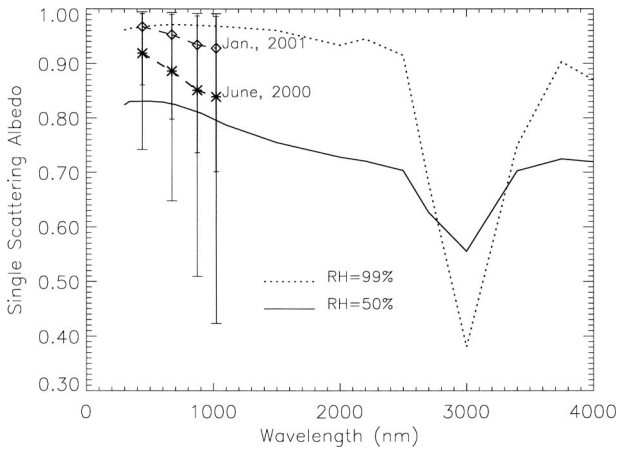

FIG. 2. The spectral single-scattering albedos of aerosol from model and the retrieved values from Cimel.

The observations in this study benefit from recent advances in technology for the measurement of broadband flux to a horizontal surface, wherein a shaded pyranometer is corrected for offset due to thermal IR exchange between its detector and dome (i.e., Bush et al. 2000; Dutton et al. 2001; Haeffelin et al. 2001) by explicit measurement of dome temperature with a thermistor. While Payne (1972) used an unshaded pyranometer to measure downwelling insolation, our record of surface insolation is obtained from the component sum method recommended by the World Meterological Organization's Baseline Surface Radiation Network (BSRN; Ohmura et al. 1998). The component sum method combines separate measurements for the direct (direct normal incident (CH1 pyrheliometer)) and diffuse (shaded pyranometer) beams. COVE adheres to the BSRN protocols for operation and calibration.

3. Radiative transfer model

The discrete ordinate method (DOM; Chandrasekhar 1960; Stamnes et al. 1988) was used to solve the radiative transfer equation in the atmosphere and ocean system. The main difference in solving the radiative transfer equation consistently in such a coupled system, from a solution that treats only the atmosphere, is caused by the refractive index change across the air–water interface. This refractive index discontinuity at the air–water interface changes the formulation of the radiative transfer equation and complicates the interface radiance continuity conditions and therefore gives rise to a different solution of the radiative transfer equation. A detailed theoretical derivation of the radiative transfer equations and their solutions were given in Jin and Stamnes (1994). Here we present only a brief description. Since we focus on the radiative energy computation for which only fluxes or irradiances are needed, we start with the azimuthally averaged version of the equation for radiative transfer (Chandrasekhar 1960)

$$\mu\frac{dI(\tau,\mu)}{d\tau} = I(\tau,\mu) - \frac{a(\tau)}{4}\int_{-1}^{1} p(\tau,\mu',\mu)I(\tau,\mu')\,d\mu' - Q(\tau,\mu), \tag{1}$$

where μ is the cosine of the polar angle, τ is the optical depth, $I(\tau,\mu)$ is the azimuthally averaged radiance, $a(\tau)$ the single scattering albedo, and $p(\tau,\mu',\mu)$ the scattering phase function. The second term on the right-hand side in Eq. (1) represents multiple scattering, while the third term $Q(\tau,\mu)$ denotes the original energy source (here the solar incidence). Because we will focus on solar radiation, the thermal source has not been taken into account here. Thus, the source term is due entirely to the solar radiation incident at the top of atmosphere, and it can be expressed as

$$Q_A(\tau,\mu) = \frac{a(\tau)}{4\pi}F\left[p(\tau,-\mu_0,\mu)\exp\left(-\frac{\tau}{\mu_0}\right) + R(\mu_0,n)p(\tau,\mu_0,\mu) \times \exp\left(-\frac{2\tau_A-\tau}{\mu_0}\right)\right] \tag{2a}$$

in the atmosphere and as

$$Q_O(\tau,\mu) = \frac{a(\tau)}{4\pi}\frac{\mu_0}{\mu_{0n}}FT(\mu_0,n) \times p(\tau,-\mu_{0n},\mu)\exp\left(-\frac{\tau_A}{\mu_0}\right)\exp\left(\frac{\tau_A-\tau}{\mu_{0n}}\right) \tag{2b}$$

in the ocean (Jin and Stamnes 1994). Here F is the solar normal irradiance at the TOA; τ_A is the total optical depth of the atmosphere; μ_0 and μ_{0n} are the cosines of solar zenith angle (SZA) seen in the atmosphere and in the ocean, respectively; and $R(\mu_0,n)$ and $T(\mu_0,n)$ are, respectively, the Fresnel reflectance and transmittance at the air–water interface. Thus, the first term on the right-hand side of Eq. (2a) represents the downward incident solar beam source, while the second term represents the upward beam source reflected back from the air–water interface due to the change in the refractive index across the interface. The method of solving Eq. (1), including the proper application of the interface and boundary conditions, has been described by Jin and Stamnes (1994). The direct solution is

$$I_p(\tau,\mu_i^a) = \sum_{j=1}^{N_1}\{C_{-jp}G_{-jp}(\mu_i^a)\exp[-k_{-jp}(\tau_p-\tau)] + C_{jp}G_{jp}(\mu_i^a)\exp[-k_{-jp}(\tau-\tau_{p-1})]\} + Z_p^0(\mu_i^a)\exp\left(-\frac{\tau}{\mu_0}\right) + Z_p^{01}(\mu_i^a)\exp\left(-\frac{2\tau_A-\tau}{\mu_0}\right), \qquad i = \pm1,\ldots,\pm N_1, \tag{3}$$

for a layer denoted by p in the atmosphere, and it is

$$I_p(\tau,\mu_i^o) = \sum_{j=1}^{N_2}\{C_{-jp}G_{-jp}(\mu_i^o)\exp[-k_{-jp}(\tau_p-\tau)] + C_{jp}G_{jp}(\mu_i^o)\exp[-k_{-jp}(\tau-\tau_{p-1})]\} + Z_p^{02}(\mu_i^o)\exp\left(-\frac{\tau}{\mu_{0n}}\right), \qquad i = \pm1,\ldots,N_2, \tag{4}$$

for a layer denoted by p in the ocean. The μ_i^a are the quadrature angles in the atmosphere, and the μ_i^o are the quadrature angles in the ocean. Here N_1 and N_2 are the numbers of the discrete quadrature points (streams) applied when replacing the integral over angle in Eq. (1) by numerical quadrature. Thus, unlike the solution for radiative transfer in the atmosphere only, the stream number and the quadrature points are not the same for

each layer in the solution of the coupled atmosphere–ocean system. The terms k_{jp} and G_{jp} are the eigenvalues and eigenvectors, respectively, associated with the solution of the homogeneous version of Eq. (1), whereas Z is related to the particular solutions due to the source term Q, and the C_{jp} are coefficients to be determined from the interface and boundary conditions.

Using the solutions expressed by Eqs. (3) and (4), the downwelling (E_d) and upwelling (E_u) irradiances can be computed according to the following formulas (Stamnes et al. 1988):

$$E_d(\tau) = 2\pi \int_0^1 \mu I(\tau, -\mu)\, d\mu = 2\pi \sum_{i=1}^{N} w_i \mu_i I(\tau, -\mu_i), \quad (5)$$

$$E_u(\tau) = 2\pi \int_0^1 \mu I(\tau, \mu)\, d\mu = 2\pi \sum_{i=1}^{N} w_i \mu_i I(\tau, \mu_i). \quad (6)$$

Because the radiative transfer equation is solved in the atmosphere and the ocean consistently, and the refractive index change at the air–water interface is included in the solution analytically, the model treats the ocean layers simply as though they were additional atmospheric layers with significantly different optical properties. The model can use a finite ocean depth for shallow waters when the reflectance properties of the ocean bottom need to be specified. We have assumed a simple Lambertian surface for the bottom.

The wind-blown ocean surface roughness is modeled using the Cox and Munk (1954) surface slope distribution for a given wind speed (Jin and Simpson 1999). Basically, the sea surface is resolved into a grid of wave facets with random slopes that follow a specified probability distribution. From Cox and Munk (1954), this probability function is

$$p(\tan\theta_n) = \frac{1}{\pi\sigma^2} \exp\left(-\frac{\tan^2\theta_n}{\sigma^2}\right), \quad (7)$$

where θ_n is the facet tilt angle (the angle between the normal to the facet and the normal to the level surface). The distribution width is σ and is related to the wind speed (U in m s^{-1}) as

$$\sigma^2 = 0.003 + 0.00512U. \quad (8)$$

Larger σ indicates more facets with large inclination. Horizontal facets ($\theta_n = 0$) always have the largest probability and the probability decreases exponentially as the slope increases.

The surface roughness alters both the reflected (back into the atmosphere) and the refracted (down into the ocean) light at the air–water interface. Reflection and refraction of light at each facet are calculated following Fresnel's law and Snell's law as for a flat surface. Therefore, given the wind speed (or given the slope distribution) and the direction of incidence, the reflected and the refracted radiation at the ocean surface can be determined.

4. Model input

The coupled radiative transfer model described above considers the absorption and scattering by atmospheric gases, clouds, and aerosols in the atmosphere and by water molecules and soluble (DOM) and particulate (phytoplankton) materials in the ocean. These optical properties are either directly from measurement data, indirectly derived/parameterized from the relevant physical properties observed, or adopted from standard models or climatological data.

In this study, the profiles of temperature, pressure, and gaseous concentrations (except for water vapor) in the atmosphere are adopted from the midlatitude atmospheric model of McClatchey et al. (1972). The wind speeds are taken from NOAA observations at COVE. The aerosol optical depth (AOD) and the total PW were from the AERONET (Cimel sun photometer) observations (Holben et al. 1998) also at COVE. However, the vertical distribution of water vapor still follows that defined in the model atmosphere. The vertical profile, single-scattering albedo and asymmetry factor of aerosols are based on MODTRAN (Berk et al. 1989) and climatological data (D'Almeida et al. 1991). Due to the proximity (25 km) of the COVE site to the city of Viginia Beach, we assumed that the aerosol is mixture of maritime aerosol and urban aerosol with each contributed a half to the total AOD observed. Based on such an assumped partition, Fig. 2 shows the single-scattering albedo produced by this assumption as a function of wavelength at relative humidities (RHs) of 50% and 99%. Asterisks (wide error bars) and diamonds (thinner error bars) in Fig. 2 represent the single-scattering albedos retrieved (Dubovik and King 2000) with Cimel data at four wavelengths for January 2001 and for June 2000, respectively. The modeled single-scattering albedos for RH of 50% and 99% are within the wide error bars of the retrievals. Precise interpretation is difficult, however, as the retrievals represent effective values for the vertical column of the atmosphere, over which the RH typically varies considerably. The simplified aerosol model could be different from the actual situation and should be justified as more relevant and more accurate data are available.

The solar spectrum considered (0.25–4.0 μm) is divided into 24 bands. In each spectral band, the molecular absorption by four trace gases (water vapor, carbon dioxide, ozone, and oxygen) in the atmosphere is considered (Tsay et al. 1989) and parameterized by the exponential-sum fitting of transmission (ESFT) method (Wiscombe and Evans 1977). The absorption by other minor trace gases is small and neglected in this study.

The ESFT method approximates the transmission function at each spectral interval (for which Beer's law does not apply) to a series of monochromatic problems. Compared with the results from the Intercomparison of Radiative Codes in Climate Models (ICRCCM) (Fouquart et al. 1991) for cases of clear sky conditions including molecular scattering and with 0.2 surface albedo, the maximum difference between our model and the average of the ICRCCM is 4.8 W m^{-2} for the downward fluxes reaching the surface through standard atmospheres and is -10.4 W m^{-2} for the total atmospheric absorption, which are 1.4% and -3.0% relative to the TOA downwelling flux, respectively. The atmospheric absorption is smaller than the ICRCCM average, which indicates that the gas absorption might be underestimated in the parameterization. It should be noted that large differences exist among the models in ICRCCM, which varied over 60 W m^{-2} in both the downward flux at the surface and the total atmospheric absorption.

In the ocean, scattering and absorption coefficients of seawater are taken from Smith and Baker (1981), who provide values applicable to the 0.2–0.8-μm region. For wavelengths larger than 0.8 μm, only absorption is considered because the scattering is weak and absorption is dominant. The absorption coefficients for oceanic particulates and DOM, and the scattering coefficients for particulates were parameterized according to bio-optical models of Gordon–Morel (1983) and Morel (1991). This parameterization was applied for inherent optical properties of the so-called Case 1 waters, for which phytoplankton and their derivatives play a predominant role in determining the optical properties. Having neither a similar model for the Case 2 (coastal) waters, nor a complete set of in situ measurements for these inherent optical properties at COVE, we here assumed the Gordon–Morel parameterization is still applicable for the waters at the COVE site. The spectral absorption of DOM is defined as (Bricaud et al. 1981).

$$a(\lambda) = a(\lambda_0) \exp[-0.014(\lambda - \lambda_0)], \qquad (9)$$

where $a(\lambda_0)$ is the DOM absorption coefficient at $\lambda_0 = 440$ nm. The phase function of phytoplankton particulates is based on the volume-scattering function measured by Petzold (1972).

The spectral chlorophyll-specific absorption coefficient was from G. Cota's measurements at the COVE in 1996 and 2000 (Cota 2001, personal communication). The chlorophyll (Chl) concentrations are based on reported monthly averaged data over 4 yr (1984–98) at the mouth of Chesapeake Bay.

5. Data analysis and comparison with model

A full year (1 March 2000–1 March 2001) of data for the downwelling and upwelling irradiances measured at the Chesapeake Bay COVE site has been analyzed. These observations have been screened for clear skies with the Long and Ackerman (2000) algorithm, which is based on a minute-by-minute analysis for each 30-min block of surface broadband data. Because the shadowing from the lighthouse frame affects the morning observations of radiation reflected by the sea, only the afternoon data was used. Using the input parameters and model described above, Figs. 3–6 show the model observation comparisons for the broadband downwelling and upwelling irradiances and the ocean surface albedo for every 3 months spanning from 1 March 2000 to 1 March 2001. The observations are 30-min averages, and the model uses an appropriate time-averaged solar zenith angle to simulate this. Wind data are also 30-min averaged. In the figures, the observations are represented by the diamond, while the model results are represented by the plus symbol. The two numbers in each panel are the mean differences between the model and the observation (model − observation) and the standard deviation (STD) of this difference, respectively. The minimum, maximum, and mean values of the corresponding wind speed, aerosol optical depth, and the total precipitable water are given in the lower-right panel in each figure.

The standard deviations of differences between the model and observations for downwelling irradiance are larger in the spring–summer seasons (Figs. 3 and 4), when the average aerosol loading is higher, than those in the fall–winter seasons (Figs. 5 and 6), when the average aerosol loading is lower. Of course, the larger TOA solar insolation in the spring–summer is partially responsible for the higher STD, but the relative standard deviation differences to the downwelling fluxes [3.18%, 2.12%, 1.77%, and 1.71% for Figs. 3–6 (not shown), respectively], which remove the effect of seasonally varying TOA, give the same indication. This indicates that the aerosol is an important contributor to the discrepancy between modeled and observed downwelling irradiance. Unlike the downwelling irradiance, the upwelling irradiance does not simply increase with the solar elevation; instead it presents a nonmonotonic relationship with SZA. For high solar elevations, the observed upwelling irradiances show a great fluctuation (the upper-right panel in Fig. 4), possibly because the sun-glint regions for those near overhead incident conditions were too close to the lighthouse frame, which affects the sea surface state (e.g., waves and foam forming), and therefore the reflectance. At fixed values of the SZA, there are seasonal variations in the upwelling irradiances and albedos. For example, at cos(SZA) values of approximately 0.5 the upwelling irradiances in the summer (Fig. 4) are generally less than 40 W m^{-2}, whereas a great many during winter (Fig. 6) exceed 40 W m^{-2} with some over 50 W m^{-2}. Some of the factors accounting for this difference are included in the model simulation, and the model captures much of this seasonal effect. At fixed SZA, incoming TOA insolation is higher during winter due to changes in the earth–sun distance. And during winter, transmission through the clear atmosphere is higher, because of reduced path-

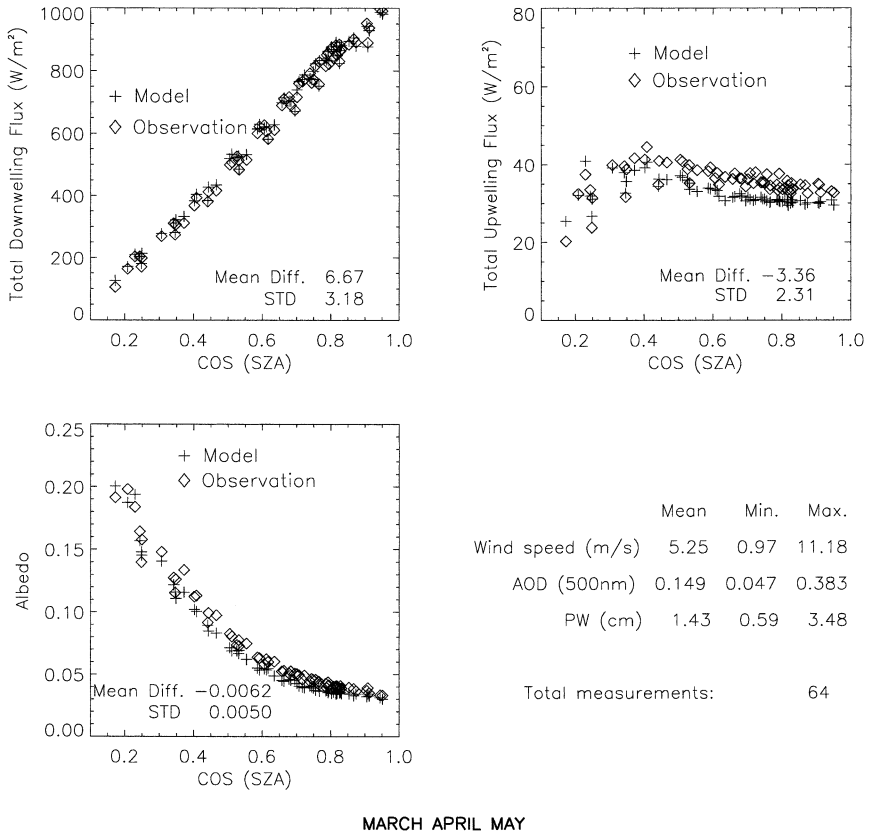

FIG. 3. Model–observation comparison for downwelling and upwelling fluxes and albedo at COVE for the 3 months from Mar to May 2000. The minimum, maximum and mean values of the corresponding wind speed, AOD, and the total PW are given in the lower-right panel.

lengths of water vapor and aerosol (both have roughly a factor of 4 difference between January and July at COVE). So at a fixed value of solar elevation, the mean surface insolation in clear conditions is larger during winter. Further, the winter insolation is relatively richer in visible (rather than near infrared) flux at the surface; the visible is more readily scattered by the sea and has higher reflectance. These factors push upwelling irradiance and ocean surface albedo toward higher values during winter. But for any given solar elevation, the ratio of direct to diffuse radiation at the ocean surface is smaller for the atmosphere with a larger amount of aerosol scattering; this can push the albedo higher or lower, depending on the effective angle of the incoming radiation. The dependence of albedos on solar zenith angle weakens with the addition of (scattering) aerosol. While the model includes seasonally varying concentrations of chlorophyll, other suspended particles that also vary seasonally have not been inserted. For all seasons, modeled upwelling irradiances are usually less than observed irradiances, and mean differences in albedo are less than 0.01. There is no conspicuous error signal associated with the seasonal effluent from the Chesapeake Bay, which peaks from April to June. The general model underestimation of the ocean surface albedo is likely due to scattering by air bubbles and other suspended nonpigment particles that were not taken into account.

As presented above, the aerosol could be an important factor for the downwelling irradiance and the wind speed could be one of the important parameters for the upwelling irradiance. Figure 7 shows these effects for the entire year of data. Figure 7(a-1) is the model observation comparison for the downwelling irradiances with observed AOD less than 0.1, and Fig. 7(a-2) is for those with AOD larger than 0.1. Although the mean model–observation difference for the downwelling irradiance is relatively small (4.12 W m^{-2}) for the whole dataset (Fig. 7a), the standard deviation of the difference is much larger (7.90 W m^{-2}). The magnitude of the STD difference in downwelling irradiance for larger AOD Fig. 7(a-2) is much larger than that for small AOD Fig. 7(a-1). Figures 7(b-1) and 7(b-2) are for the model–observation comparison for the upwelling irradiance for wind speed less and for wind speed larger than 10 m s^{-1}, respectively. In both wind speed categories, the mean model results are less than the observations, but all model results for wind speed larger than 10 m s^{-1} are less than the observations with larger mean bias. However, though the mean model–observation discrep-

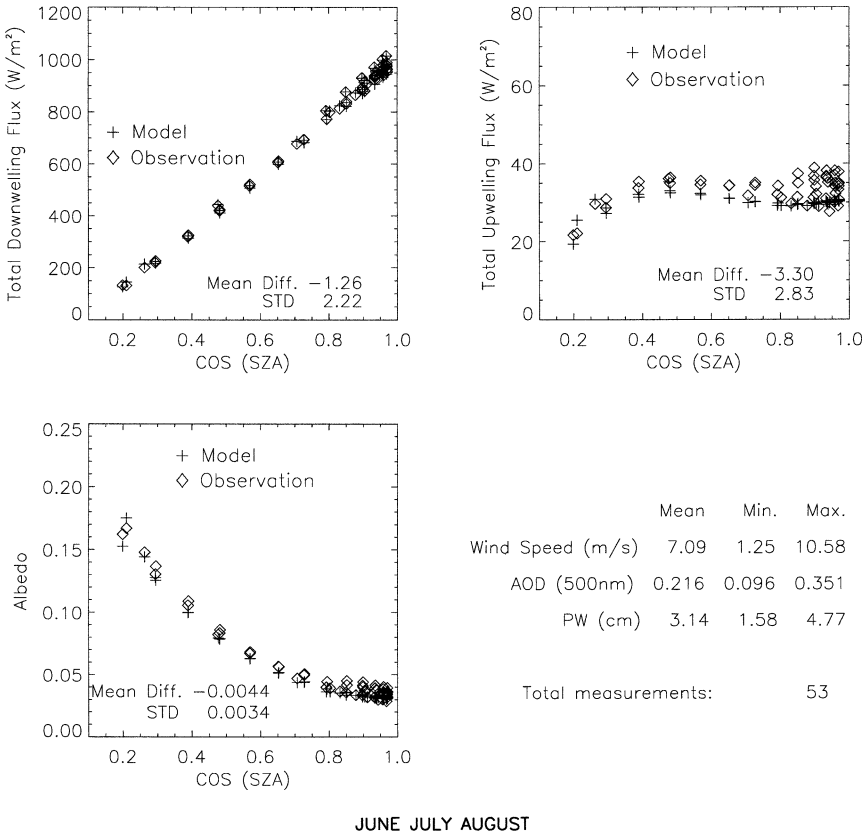

FIG. 4. Same as Fig. 3 but for the 3 months from Jun to Aug 2000.

ancies in the upwelling irradiance for high wind speeds are larger than those for low winds, the model–observation discrepancies for the upwelling flux are not simply related to the wind speed monotonically. It seems that the wind speed [in terms of the wind effect on sea surface slopes as described by the Cox–Munk (1954) model] is not the main factor for the model–observation differences of the upwelling flux.

Figure 8 shows the differences between model simulations and observations for the direct normal component (Figs. 8a and 8a-1) and the diffuse component (Figs. 8b and 8b-1) of the downwelling irradiances, respectively. Figures 8a and 8b include the whole year of data for all AOD, whereas Figs. 8a-1 and 8b-1 include only the data with AOD less than 0.1. For all AOD during the year, the difference as model minus observation for the direct normal is -13.45 W m^{-2}. The negative bias is in part due to the differing fields of view (FOVs) of the Cimel spectral photometer (1.2°) and the CH1 broadband pyrheliometer (5.7°). As the photometer FOV is smaller, it tends to give a higher value for AOD than would the pyrheliometer FOV (Kinne et al. 1998 described a similar, but more pronounced effect for cirrus particles). For example, a ray scattered 2° from incident is beyond the Cimel FOV (1.2°) and would be counted as AOD by the photometer; but the larger pyrheliometer FOV (5.7°) would consider this same ray as a component of the unscattered incident beam. As the radiative transfer code uses the Cimel AOD, it scatters more out of the direct normal beam than is measured by the pyrheliometer (giving negative biases of -13.45 W m^{-2} in Fig. 8a and -10.21 W m^{-2} in Fig. 8a-1). Because the shading ball of the diffuse pyranometer is approximately consistent with that of the pyrheliometer, the same effect contributes part of the slight positive biases for the computed diffuse downwelling irradiance (12.21 W m^{-2} in Fig. 8b and 9.14 W m^{-2} in Fig. 8b-1). Note that the temporal domains of Figs. 7a, 8a, and 8b are not identical; each consists of those intervals having clear skies and quality measurements (from the pyrheliometer in Fig. 8a, from the shaded pyranometer in 8b, and from both instruments in 7a).

Figure 9 shows the effects of wind on the ocean surface albedo. The three symbols in Fig. 9a display the observed albedo at COVE for three wind speed ranges, respectively. The dotted line is the modeled albedo with the minimum observed wind (0.48 m s^{-1}) of the dataset, whereas the solid line is modeled albedo with the maximum observed wind (14.0 m s^{-1}). The midlatitude atmospheric model with measured mean PW (1.39 cm) and mean AOD (0.1) for the observations was used in the model simulations. The modeled albedos for the two wind speeds differ only slightly when the cosine of SZA is larger than 0.5 (SZA = 60°), but the difference in-

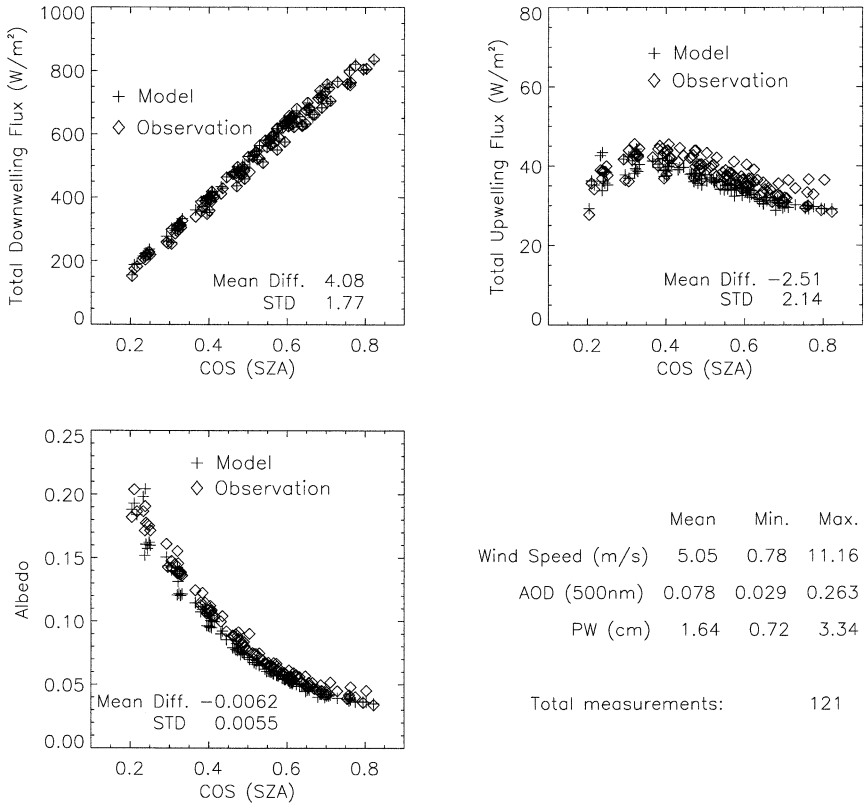

FIG. 5. Same as Fig. 3 but for the 3 months from Sep to Nov 2000.

creases rapidly for SZA larger than 60°. This suggests that the wind effects on the surface albedo are most likely to be observed at low solar elevations (i.e., where both the magnitude and scatter of the observed albedos are large). The observations show the same relations between the albedo and the SZA and wind speed (i.e., the observed albedo at the low suns are the highest for small winds and the lowest for large winds) as the model, though the atmospheric conditions (e.g., PW and AOD) varied widely for the observations and affected the albedo significantly. The good correspondence of model and measurements suggests that the measurements are of high quality and the theory is sound.

Figure 9b shows differences of surface albedo as model minus observation for the same three wind speed ranges as in Fig. 9a. The model calculations in Fig. 9b were made for each observation separately with measured PW and AOD as presented in Figs. 3–6. Figure 9b shows that the mean albedo differences for all wind speed categories are negative (model less) and with similar STD magnitude. As the discrepancies between model and observation show no relationship to wind speed over a large range of SZA, we infer that the general bias in the model (a low surface albedo) is not due to the treatment of wind on the orientation of the reflecting sea slope facets. Most of the wind impact on optics via sea slope is caused by small capillary waves, which respond to changes in wind rapidly. Note that while the model accounts for the forcing of reflectance due to the Cox–Munk wind speed dependence of sea slopes, other wind effects, such as wind-associated low-frequency sea swell, foam, and injected air bubbles in the water, have not been included. The model has been driven with the mean wind speed observed during intervals of 30 min; but it has no provision for gustiness or peak wind, which is higher during winter. The high wind speed may contribute to ocean reflection by producing air bubbles in the water (which could be persistent) and increase the backscattering of the ocean; this is not considered in the model.

6. Discussion

a. Atmospheric aerosol

Based on the results shown above, it is observed that the model–observation agreement is better for the downwelling irradiances than for the upwelling irradiances. This is due in part to the more comprehensive observations to specify the atmospheric optical properties (on that the downwelling irradiance mainly depends) than those for the oceanic properties (on which the upwelling irradiance depends heavily). For the downwelling irradiance, the STD

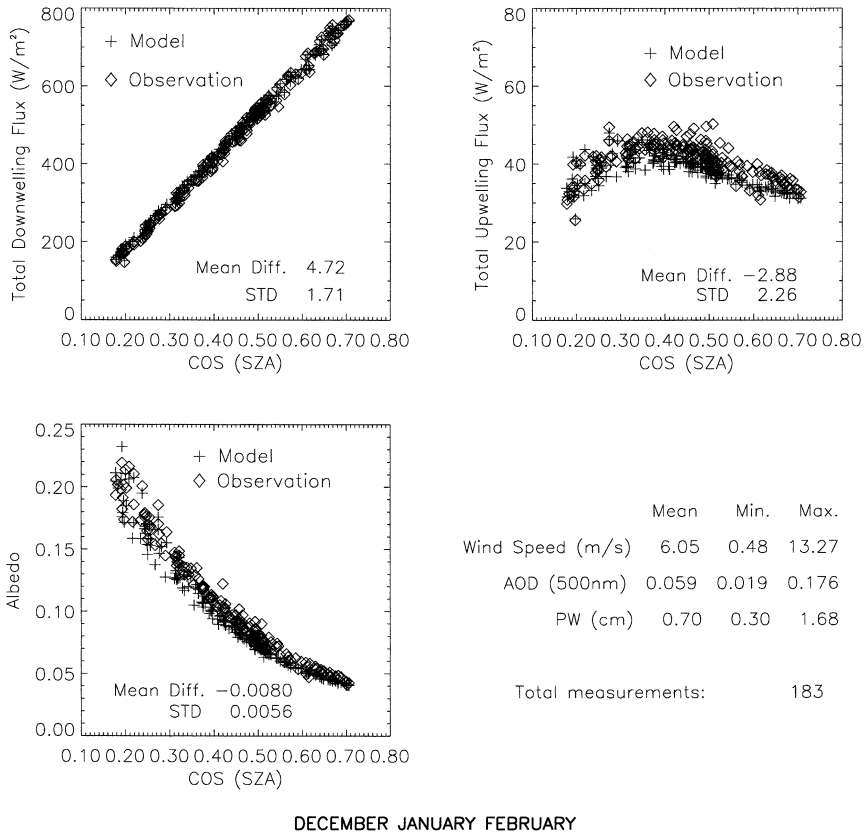

FIG. 6. Same as Fig. 3 but for the 3 months from Dec 2000 to Feb 2001.

model–observation difference is related to the uncertainties in the aerosol optical properties; this STD difference is smaller for low AOD than for high AOD. Although the AOD is from measured data, the single-scattering albedo and the scattering phase function for the aerosol are based on aerosol models (D'Almeida et al. 1991; Berk et al. 1989), which may not match the actual values and hence contribute to the model–observation difference. The aerosol optical properties are also correlated with the precipitable water. For instance, the single-scattering albedo of aerosols in the visible spectrum increases as the humidity increases. Our model has considered this variation of aerosol optical properties related to the precipitable water. Total precipitable water was also from in situ measurements. However, as the vertical distribution of the water vapor follows the standard atmospheric profile rather than the actual profile, there are further uncertainties in aerosol optical properties that affect the computed downwelling irradiances.

Here the pyrheliometer is rigorously calibrated and traceable to an international standard instrument. While we have adhered to the formal BSRN procedure for testing the shaded diffuse pyranometer, it should be noted that there is no truly rigorous method for calibrating the pyranometer measurement of diffuse irradiance. Hence comparisons of the model with observations for the direct normal component (Figs. 8a and 8a-1) in this regard constitute a stricter test bed than do the comparisons with the diffuse (Figs. 8b and 8b-1) and summed global (Figs. 7a and 7a-1) fluxes. The absolute value of the mean bias for direct (Figs. 8a and 8a-1) is smaller for low AOD (-10.21 W m^{-2}) than for all AOD (-13.45 W m^{-2}); and the standard deviation for direct is smaller for low AOD (6.15 W m^{-2}) than for all AOD (11.57 W m^{-2}). The relative STD of 1.24% for the direct downwelling irradiances for low AOD is also smaller than the relative STD of 2.06% for all AOD. The smaller bias and STD for low AOD are consistent with the hypothesis that aerosol properties beyond the spectral coverage of the Cimel are responsible for some of the discrepancies. The Cimel bands extend from 340 to 1020 nm, leaving ~30% of the solar spectrum in the UV and near IR with no AOD measurement. For this portion of the UV and near IR, we rely upon the aerosol models for input to radiative transfer calculations. When we encounter high AOD in the part of the spectrum measured by the Cimel, the impact of uncertainties in the unmeasured UV and near IR produces the larger broadband biases and STD.

b. Phytoplankton in the ocean

While the upwelling irradiance is of course affected by the value of the downwelling, it is also influenced

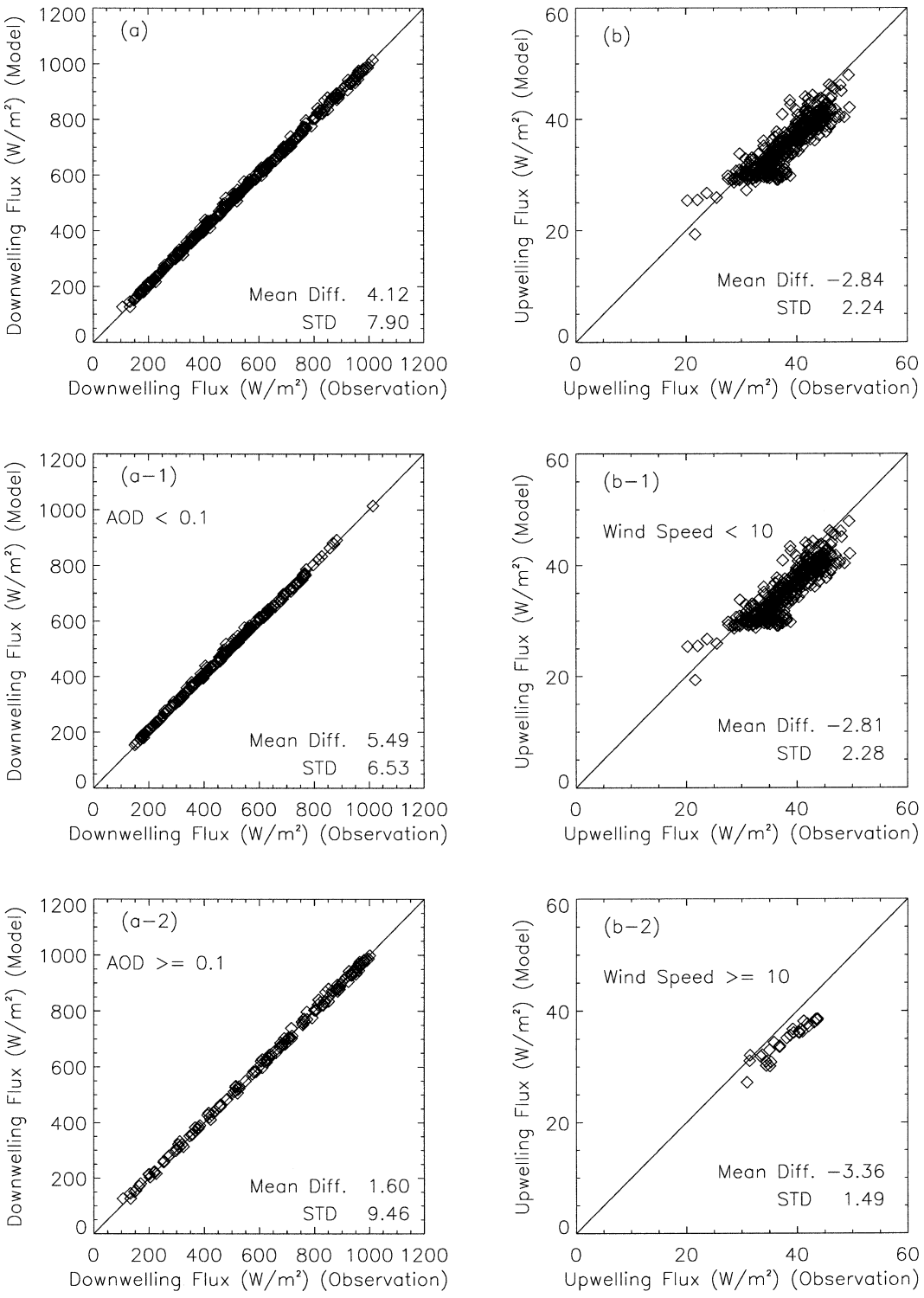

FIG. 7. Model–observation comparison for the (left) broadband downwelling and (right) upwelling for a full year of data from 1 Mar 2000 to 1 Mar 2001. All (a) AOD, (a-1) AOD < 0.1, and (a-2) AOD > 0.1. All (b) wind speed, (b-1) wind speed less than 10 m s^{-1}, and (b-2) larger than 10 m s^{-1}, respectively.

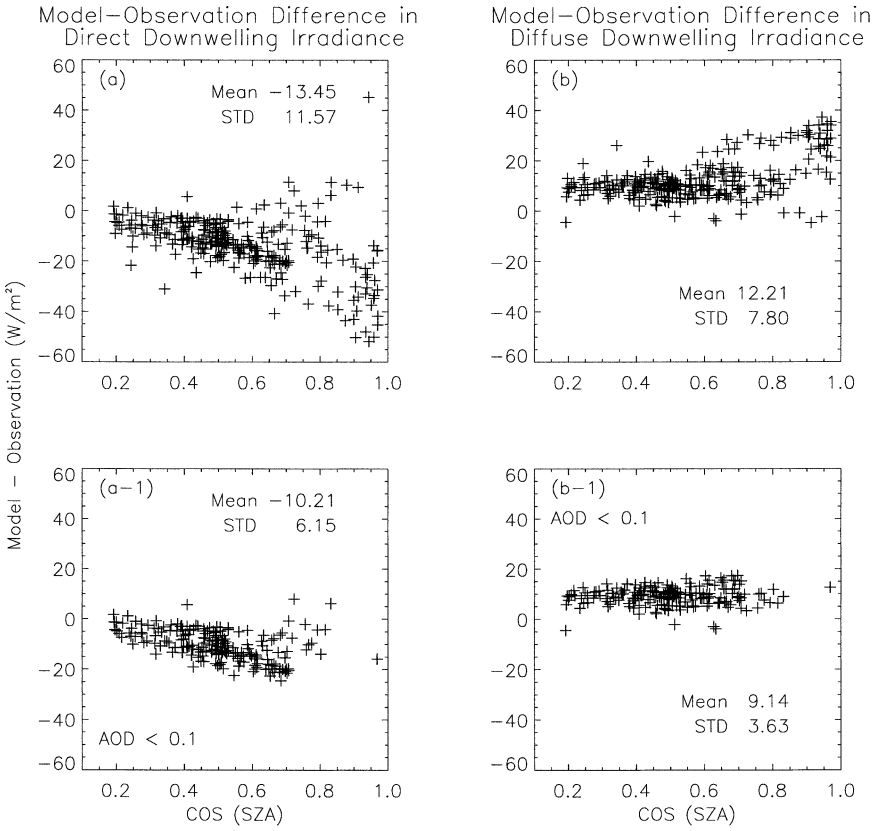

FIG. 8. Differences between model and measurement for (left) the direct and (right) the diffuse downwelling irradiance, respectively. (top) All dataset and (bottom) those observations with AOD < 0.1.

by the sea surface state, surface wind, and ocean constituents; among these, we employed temporally intensive, in situ observations for the wind speed only. The model inputs for Chl concentration were taken from monthly averaged observations at the mouth of the Chesapeake Bay (36.99°N, 76.02°W), which is 29 km away from the COVE observation site; therefore, the actual Chl concentrations could be quite different from those we used. The monthly averaged Chl concentration at COVE retrieved from SeaWiFS data for the period corresponding to the surface observations are generally less than the values we used in the model. SeaWiFS-retrieved Chl concentrations, however, have significant uncertainties, especially in coastal regions. To estimate the error in albedo from a possible bias in Chl concentration, we calculated the broadband albedo as a function of the Chl concentration at two solar zenith angles for clear sky conditions (Fig. 10). As shown in Fig. 10, the broadband ocean surface albedo is not sensitive to the Chl concentration, especially when the concentration is as high as at the COVE site. Scattering and absorption by phytoplankton vary with wavelength and nearly cancel in the broadband. Although Chl has strong absorption around 443 and 670 nm, which would reduce the broadband ocean albedo, scattering at other wavelengths tends to increase the albedo. Figure 10 shows that the broadband ocean surface albedo has a change of less than 0.005 for Chl concentration range from 0 to 10 mg m^{-3}; this easily spans the Chl variation at COVE. Therefore, uncertainties in the Chl concentration used by the model input are not the primary source for the model–observation discrepancies in the broadband upwelling irradiance and albedo over the ocean surface at COVE.

c. Whitecaps and air bubbles

We can also exclude the effect of foam as a primary source for the model–observation difference in the ocean surface albedo. Here, most of the wind speeds are less than 12 m s^{-1}, for which the whitecap contribution is negligible (Koepke 1984). Moore et al. (2000) showed that over the wind speed range 9–12 m s^{-1}, whitecaps augmented the visible reflectance by only 0.001–0.002. The impact on the broadband albedo will be even smaller because foam augmented reflectance diminishes in the near-infrared (Frouin 1996).

Because the modeled ocean surface albedo is mostly less than the observations for all seasons, wind speeds, and solar zenith angles (except for very large angles), some scattering mechanisms in the ocean, which could

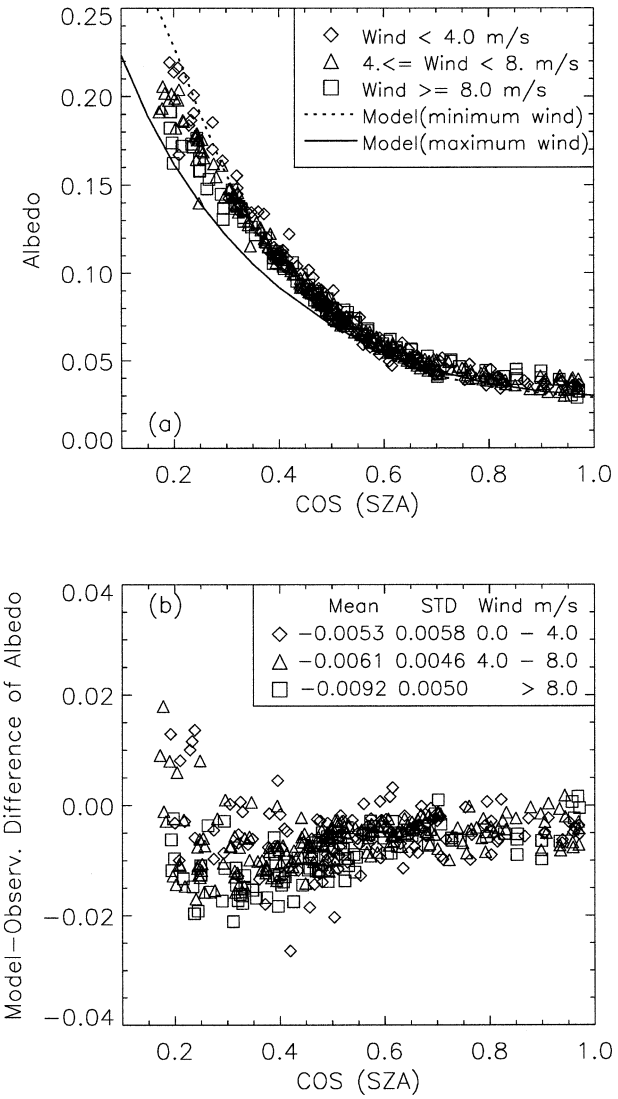

FIG. 9. Wind effects on the ocean surface albedo. (a) The observed albedo as a function of cosine of SZA in three wind categories. The dashed line and the solid line are the modeled albedo with the minimum wind (0.48 m s^{-1}) and maximum wind (14.0 m s^{-1}) of the observations, respectively. The midlatitude atmospheric model and the mean AOD and PW were used in the model calculations. (b) The albedo differences between model and observation in the three wind ranges. Here model inputs for PW and AOD varied with observations as in Figs. 2–5.

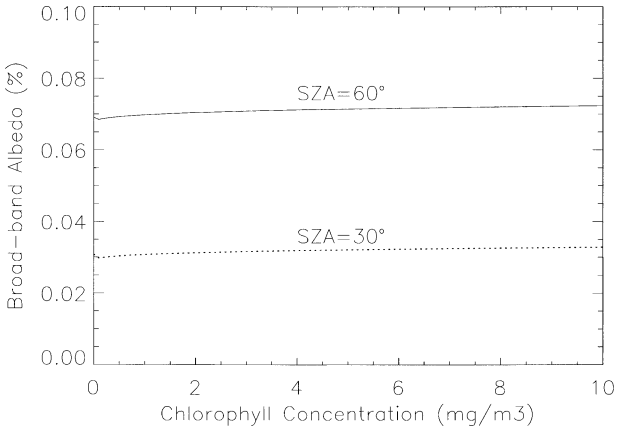

FIG. 10. The modeled broadband ocean surface albedo as a function of Chl concentration for two SZAs for clear midlatitude atmospheric conditions.

increase the ocean reflection, were likely missed in the model calculations. Scattering by the air bubbles below the ocean surface is one such mechanism. When waves break on the ocean surface they generate air bubbles and inject significant quantities of air bubbles into the ocean (Baldy 1988; Hwang et al. 1989). Larger bubbles return to the surface relatively quickly and burst, whereas smaller bubbles can persist and continue to influence ocean optics, and therefore, influence the light transportation in water where they are present. Our understanding of the relative importance of the air bubbles on the radiative transfer in the ocean is severely limited, owing in part to their complexity and in part to the lack of measurement. Pioneering research on the effects of air bubbles on the ocean surface reflectance was carried out by Stramski (1994), who performed Mie calculations of light scattering by submerged bubbles with a size distribution following the −4th power law for radii from 10 to 150 μm. Similar and more detailed calculations were followed by Zhang et al. (1998) and Flatau et al. (1998). Their results all demonstrated that the air bubbles in the ocean could increase the backscattering of ocean waters substantially, depending on the bubble properties such as coating over the bubble surface, number density, and size distribution.

Here we compute the bubble effect on the ocean surface albedo with the coupled radiative transfer model, and examine if the bubble scattering could explain the model–observation difference in the broadband albedo shown in the last section. Optical properties of air bubbles are calculated using Mie theory assuming the same power-law size distribution as Zhang et al. (1998) and no absorption. Bubble number densities of $\sim 10^5$ to $\sim 10^7$ m^{-3} are common at sea (Zhang et al. 1998; O'Hern et al. 1988). The measured number densities by several investigators listed in Zhang et al. range from 4×10^4 to 2×10^7 (m^{-3}). For the Zhang et al. size distributions, these are equivalent to air volume fractions from $\sim 10^{-3}$ per million to ~ 1.0 per million. Figure 11 compares the calculated spectral ocean surface albedos with (red lines) and without (black lines) air bubble scattering for three Chl concentrations (0.0, 0.1, and 5.0 mg m^{-3}), considered to represent, respectively, pure seawater, open ocean, and coastal ocean. A bubble number density of 1.0×10^7 (m^{-3}), SZA of 30° and the midlatitude summer atmospheric model were used for the calculations. The bubble effect on the ocean reflectance in Fig. 11 is mainly in the near UV and visible from 300 to 700 nm. Increasing Chl concentration here reduces the bubble effect on the reflectance.

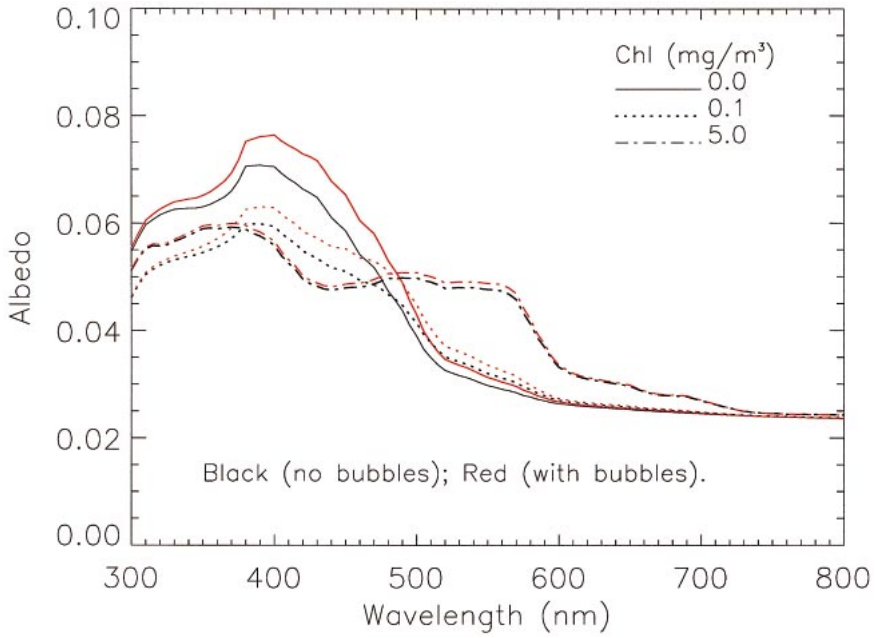

FIG. 11. The modeled spectral ocean surface albedo for two conditions—with air bubbles considered (red lines) and without bubbles considered (black lines). SZA of 30° and bubble number density of 10^7 (m^{-3}) were used in the calculations.

Figure 12 shows the change in broadband albedo as a function of the bubble number density for three different Chl concentrations; the same input parameters for the atmosphere and ocean as for Fig. 11 were used, but the SZA was 60°. The increase in albedo due to air bubbles does not change sharply with SZA. While air bubbles could account for the model–observation discrepancies (0.005–0.01) in broadband albedo, Fig. 12 shows that very high bubble number density ($>10^8$ m^{-3}) would be required to close the gap for waters with high Chl concentration as at the COVE site. Hence, we suggest that the solution is not likely to be ''missing air bubbles.''

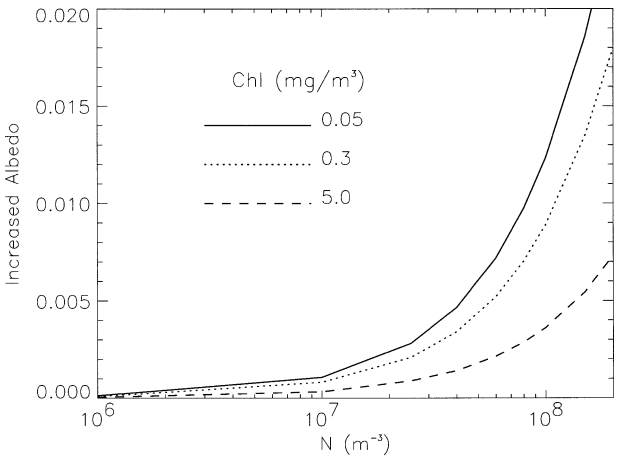

FIG. 12. The change in broadband albedo as a function of bubble number density for three different Chl concentrations and SZA of 60°.

But there is a caveat to our rejection of the bubble solution. It should be noted that we assumed a uniform distribution of the air bubbles in the water in the calculations. The actual distribution could be very complicated, usually with maximum density near the surface and decreasing with depth (Wu 1988; Baldy 1988). A maximum density near the surface would increase the albedo. We here simply conclude that our model simulations are instructive and indicate the potential role of air bubbles.

d. Suspended sediments

Another mechanism in the sea that could be important (but not considered in our calculations) is the scattering by suspended sediments. Because the COVE (11-m water depth) is only 25 km from the coast, suspended sediments are common there and would contribute to the scattering. Measurements by Gould et al. (1999) in the Chesapeake Bay showed that due to the presence of sediments, the total particle-scattering coefficients observed were much higher than those estimated from the Gorden–Morel scattering model. The scattering model (Gordon and Morel 1983; Morel 1991) relates the spectral-scattering coefficient, $b_p(\lambda)$, for ocean particulates to the Chl concentration (C in mg m^{-3}) as

$$b_p(\lambda) = \frac{550}{\lambda} 0.3 C^{0.62}. \quad (10)$$

This parameterization was developed for Case 1 waters where the particle scattering is primarily due to phy-

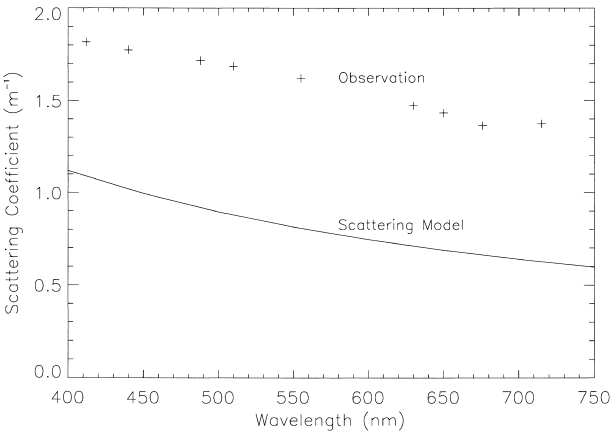

FIG. 13. Scattering coefficient based on Morel's scattering model and comparison with those from in situ observation at the mouth of Chesapeake Bay.

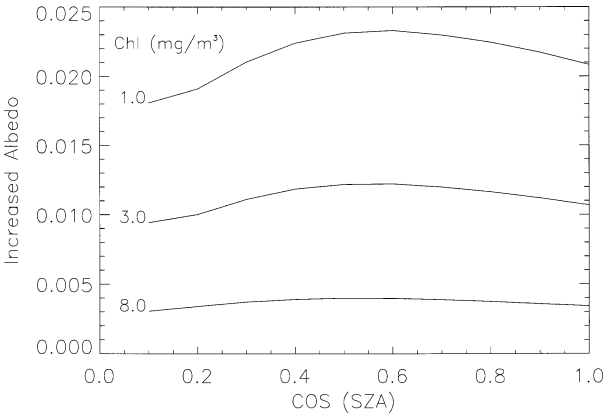

FIG. 14. The increased broadband albedo over ocean surface by using the measured scattering coefficients at the Chesapeake Bay.

toplankton and its derivatives, and it could underestimate the in-water scattering at COVE. Figure 13 shows the measured scattering coefficients at a station (36.917°N, 75.938°W) at the mouth of the Chesapeake Bay, which is 20 km from the COVE; results based on the parameterization [Eq. (10)] for Chl concentration of 5.0 mg m^{-3} are also presented. Differences between the measurement and the model are apparent in Fig. 13. To estimate the corresponding error in broadband albedo due to the sediments, we substituted our values of in-water scattering coefficients based on Eq. (10) with those measured by Gould et al. (1999). Figure 14 shows the surface albedo changes when using the measured scattering data by Gould et al. (1999) at three Chl concentrations. The results indicate that scattering by coastal sediments can easily increase the broadband albedo by 0.01 (i.e., the approximate differences between observation and theory in Figs. 2–5). However, it should be understood that the suspended sediments are affected by river discharge, bottom resuspension, and shore erosion; their concentrations and properties could vary strongly with location and time. The measured scattering data we used here are likely to be different from the actual values at COVE. In addition, these scattering data may include some contribution from bubbles. But the test results here indeed suggest that scattering by sediments is important; it could explain the model underestimation of the ocean surface albedo at COVE. The albedo biases (model minus observation) at a range of cosine of SZA are given in Table 2.

Water depth at COVE is 11 m. The sea bottom is rarely visible from the rigid steel platform 20 m above the sea surface. When the effect of bottom albedo was included in sensitivity calculations, we found that absorption and scattering by other components led to a negligible impact by the bottom albedo on the upwelling irradiance and albedo over the ocean surface. Further note that with such a shallow depth, our database at COVE does not include the largest swell amplitudes that are sometimes found in the deep ocean. Most of the variance in sea slope is due to the local wind waves, which have smaller amplitudes. The periods and amplitudes of ocean waves are observed at COVE, and an investigation of their possible impacts (beyond the local wind speed effects considered here) is a topic for future study.

7. Conclusions

To validate retrievals of solar radiation and albedo in the CERES satellite program, broadband upwelling and downwelling solar irradiances are measured routinely over the ocean at COVE. To analyze the measurements, we have applied a coupled atmosphere–ocean radiative transfer model. The coupled model treats absorption and scattering in both the atmosphere and the ocean explicitly and consistently. Therefore, the model considers the ocean layers simply as though they were just as additional atmospheric layers just with different optical properties, and can calculate the upwelling radiation from the ocean and the ocean surface albedo based on the optical properties in the air and the sea. The wind-blown ocean surface roughness is modeled using the Cox–Munk surface slope distribution for a given wind speed. Key input parameters for the model include aerosol optical depth, wind speed, and total precipitable water; these are measured at COVE together with the irradiances.

Having more comprehensive observations available to describe the atmospheric conditions than those for the ocean, we have obtained better model–observation agreement for the downwelling irradiance, which depends primarily on the atmospheric optical properties,

TABLE 2. The mean differences of albedo (model minus observation) at a range of cos(SZA).

cos(SZA)	0.0–0.2	0.2–0.4	0.4–0.6	0.6–0.8	0.8–1.0
Difference	−0.0002	−0.009	−0.008	−0.005	−0.004

than for the upwelling irradiance, which depends heavily on the ocean optical properties. The difference between the modeled results and the observations for the downwelling irradiance is related to the aerosol optical depth. A larger STD difference corresponds to larger aerosol loading, indicating that aerosols are important sources for the discrepancy between modeled and observed downwelling irradiances. At any specified solar elevation, the mean upwelling irradiances vary with season; relevant factors include the state of the atmosphere and the sea. The mean model–observation differences and the STD differences for ocean surface albedo are less than 0.01. However, the modeled upwelling irradiances (and hence the ocean surface albedo) are mostly less than the observations for all seasons, indicating that some scattering mechanisms in the ocean were missed in the model calculations. Test results show that the missed important scattering components are most likely the suspended sediments and/or air bubbles. The uncertainties in aerosol optical properties, Chl concentration, wind speed, or foams are not the primary factor for the model–observation difference in the ocean surface albedo. Including either the scattering by air bubbles and/or by suspended sediments have the potential to make up the model underestimation in the ocean surface reflection. Information on these constituents in the water are desired and further research is required. Some of these topics will be addressed in forthcoming analyses of data from the Chesapeake Lighthouse and Aircraft Measurements for Satellites field campaign. The coupled atmosphere–ocean radiative transfer modeling is online at http://snowdog.larc.nasa.gov/jin/rtset.html.

Acknowledgments. We thank Glenn Cota at ODU and Richard Gould at NRL for providing us their measurement data for ocean optical properties; B. N. Holben at NASA for providing AERONET data. Dave Rutan helped in obtaining the Chl data. Dr. G. Cota carefully read the manuscript and gave invaluable comments that helped to improve the manuscript.

REFERENCES

Baldy, S., 1988: Bubbles in the close vicinity of breaking waves: Statistical characteristics of the generation and dispersion mechanism. *J. Geophys. Res.,* **93,** 8239–8248.

Berk, A., L. S. Bernstein, and D. C. Robertson, 1989: MODTRAN: A moderate resolution model for LOWTRAN 7. Air Force Geophysics Laboratory Rep. AFGL-TR-89-0122, Hanscom, MA, 42 pp.

Bricaud, A., A. Morel, and L. Prieur, 1981: Absorption by dissolved organic matter of the sea (yellow substance) in the UV and visible domains. *Limnol. Oceanogr.,* **26,** 43–53.

Bush, B. C., F. P. J. Valero, A. Sabrina Simpson, and L. Bignone, 2000: Characterization of thermal effects in pyranometers: A data correction algorithm for improved measurement of surface insolation. *J. Atmos. Oceanic Technol.,* **17,** 165–175.

Chandrasekhar, S., 1960: *Radiative Transfer.* Dover, 393 pp.

Charlock, T. P., and T. L. Alberta, 1996: The CERES/ARM/GEWEX Experiment (CAGEX) for the retrieval of radiative fluxes with satellite data. *Bull. Amer. Meteor. Soc.,* **77,** 2673–2683.

Chou, M.-D., and W. Zhao, 1997: Estimation and model validation of surface solar radiation and cloud radiative forcing using TOGA COARE measurements. *J. Climate,* **10,** 610–620.

Conant, W. C., V. Ramanathan, F. P. J. Valero, and J. Meywerk, 1997: An examination of the clear-sky solar absorption over the central equatorial pacific: Observations versus models. *J. Climate,* **10,** 1874–1884.

Cox, C., and W. Munk, 1954: Measurement of the roughness of the sea surface from photographs of the sun's glitter. *J. Opt. Soc. Amer.,* **44,** 838–850.

D'Almeida, G. A., P. Koepke, and E. P. Shettle, 1991: *Atmospheric Aerosols: Global Climatology and Radiative Characteristics.* A. Deepak, 561 pp.

Dubovik, O., and M. D. King, 2000: A flexible inversion algorithm for retrieval of aerosol optical properties from sun and sky radiance measurements. *J. Geophys. Res.,* **105,** 20 673–20 696.

Dutton, E. G., J. J. Michalsky, T. Stoffel, B. W. Forgan, J. Hickey, D. W. Nelson, T. L. Alberta, and I. Reda, 2001: Measurement of broadband diffuse solar irradiance using current commercial instrumentation with a correction for thermal offset errors. *J. Atmos. Oceanic Technol.,* **18,** 297–314.

Flatau, P. J., M. Flatau, J. R. V. Zaneveld, and C. D. Mobley, 1998: Radiative transfer properties of bubble clouds in seawater. *Quart. J. Roy. Meteor. Soc.,* **124,** 1–20.

Fouquart, Y., B. Bonnel, and V. Ramaswamy, 1991: Intercomparing shortwave radiation codes for climate studies. *J. Geophys. Res.,* **96,** 8955–8968.

Frouin, R., M. Schwindling, and P.-Y. Deschamps, 1996: Spectral reflectance of sea foam in the visible and near-infrared: In situ measurements and remote sensing implications. *J. Geophys. Res.,* **101,** 14 361–14 371.

Gordon, H. R., and A. Morel, 1983: *Remote Assessment of Ocean Color for Interpretation of Satellite Visible Imagery: A Review.* Springer-Verlag, 114 pp.

Gould, R. W., Jr., R. A. Arnone, and P. M. Martinolich, 1999: Spectral dependence of the scattering coefficient in case 1 and case 2 waters. *Appl. Opt.,* **38,** 2377–2383.

Haeffelin, M., S. Kato, A. M. Smith, K. Rutledge, T. Charlock, and J. R. Mahan, 2001: Determination of the thermal offset of the Eppley Precision Spectral Pyranometer. *Appl. Opt.,* **40,** 472–484.

Holben, B. N., and Coauthors, 1998: AERONET—A federated instrument network and data archive for aerosol characterization. *Remote Sens. Environ.,* **66,** 1–16.

Houghton, J. T., L. G. Meira Filho, B. A. Callander, N. Harris, A. Kattenberg, and K. Maskell, Eds.,1996: *Climate Change 1995: The Science of Climate Change.* Cambridge University Press, 572 pp.

Hwang, P. A., D. Xu, and J. Wu, 1989: Breaking of wind-generated waves: Measurements and characteristics. *J. Fluid Mech.,* **202,** 177–200.

Jin, Z., and J. J. Simpson, 1999: Bidirectional anisotropic reflectance of snow and sea ice in AVHRR channel 1 and 2 spectral regions. Part I: Theoretical analysis. *IEEE Trans. Geosci. Remote Sens.,* **37,** 543–554.

——, and K. Stamnes, 1994: Radiative transfer in nonuniformly refracting layered media: Atmosphere–ocean system. *Appl. Opt.,* **33,** 431–442.

Kato, S., T. P. Ackerman, E. E. Clothiaux, J. H. Mather, G. G. Mace, M. L. Wesely, F. Murcray, and J. Michalsky, 1997: Uncertainties in modeled and measured clear-sky surface shortwave irradiances. *J. Geophys. Res.,* **102,** 25 881–25 898.

Kinne, S., R. Bergstrom, O. B. Toon, E. Dutton, and M. Shiobara, 1998: Clear-sky atmospheric solar transmission: An analysis based on FIRE 1991 field experiment data. *J. Geophys. Res.,* **103,** 19 709–19 720.

Koepke, P., 1984: Effective reflectance of oceanic whitecaps. *Appl. Opt.,* **23,** 1816–1824.

Long, C. N., and T. P. Ackerman, 2000: Identification of clear skies from broadband pyranometer measurements and calculation of

downwelling shortwave cloud effects. *J. Geophys. Res.*, **105,** 15 609–15 626.
McClatchey, R. A., R. W. Fenn, J. E. A. Selby, F. E. Volz, and J. S. Garing, 1972: Optical properties of the atmosphere. AFCRL Rep. 72-0497. Air Force Cambridge Laboratories, Bedford, MA, 113 pp.
Moore, K. D., K. J. Voss, and H. R. Gordon, 2000: Spectral reflectance of whitecaps: Their contribution to water-leaving radiance. *J. Geophys. Res.*, **105,** 6493–6499.
Morel, A., 1991: Light and marine photosynthesis: A spectral model with geochemical and climatological implications. *Progress in Oceanography,* Vol. 26, Pergamon, 263–306.
O'Hern, T. J., L. d'Agostino, and A. J. Acosta, 1988: Comparison of holographic and Coulter counter measurements of cavitation nuclei in the ocean: Transactions of the ASME. *J. Fluids Eng.*, **110,** 200–207.
Ohmura, A., and Coauthors, 1998: Baseline Surface Radiation Network (BSRN/WCRP): New precision radiometry for climate research. *Bull. Amer. Meteor. Soc.*, **79,** 2115–2136.
Payne, R. E., 1972: Albedo of the sea surface. *J. Atmos. Sci.,* **29,** 959–970.
Petzold, T. J., 1972: Volume scattering functions for selected ocean waters. Scripps Institution of Oceanography Ref. 72-78, 79 pp.
Smith, R. C., and K. S. Baker, 1981: Optical properties of the clearest natural waters (200–800 nm). *Appl. Opt.*, **20,** 177–184.
Stamnes, K., S. C. Tsay, W. J. Wiscombe, and K. Jayaweera, 1988: Numerically stable algorithm for discrete-ordinate-method radiative transfer in multiple scattering and emitting layered media. *Appl. Opt.*, **27,** 2502–2509.
Stramski, D., 1994: Gas microbubbles: An assessment of their significance to light scattering in quiescent seas. *Ocean Optics XII,* J. S. Jaffe, Ed., Proceedings of SPIE series, Vol. 2258, SPIE, 704–710.
Tsay, S. C., K. Stamnes, and K. Jayaweera, 1989: Radiative energy budget in the cloudy and hazy Arctic. *J. Atmos. Sci.*, **46,** 1002–1018.
Wiscombe, W. J., and J. W. Evans, 1977: Exponential-sum fitting of radiative transmission functions. *J. Comput. Phys.*, **24,** 416–444.
Wu, J., 1988: Bubbles in the near-surface ocean: A general description. *J. Geophys. Res.*, **93,** 587–590.
Zhang, X., M. Lewis, and B. Johnson, 1998: Influence of bubbles on scattering of light in the ocean. *Appl. Opt.*, **37,** 6525–6536.